Cation-induced kinetic heterogeneity of the intron–exon recognition in single group II introns

Danny Kowerko[1], Sebastian L. B. König[1,2], Miriam Skilandat, Daniela Kruschel[3], Mélodie C. A. S. Hadzic, Lucia Cardo[4], and Roland K. O. Sigel[5]

Department of Chemistry, University of Zurich, 8057 Zurich, Switzerland

Edited by D. Thirumalai, University of Maryland, College Park, MD, and accepted by the Editorial Board February 3, 2015 (received for review December 6, 2013)

RNA is commonly believed to undergo a number of sequential folding steps before reaching its functional fold, i.e., the global minimum in the free energy landscape. However, there is accumulating evidence that several functional conformations are often in coexistence, corresponding to multiple (local) minima in the folding landscape. Here we use the 5′-exon–intron recognition duplex of a self-splicing ribozyme as a model system to study the influence of Mg^{2+} and Ca^{2+} on RNA tertiary structure formation. Bulk and single-molecule spectroscopy reveal that near-physiological M^{2+} concentrations strongly promote interstrand association. Moreover, the presence of M^{2+} leads to pronounced kinetic heterogeneity, suggesting the coexistence of multiple docked and undocked RNA conformations. Heterogeneity is found to decrease at saturating M^{2+} concentrations. Using NMR, we locate specific Mg^{2+} binding pockets and quantify their affinity toward Mg^{2+}. Mg^{2+} pulse experiments show that M^{2+} exchange occurs on the timescale of seconds. This unprecedented combination of NMR and single-molecule Förster resonance energy transfer demonstrates for the first time to our knowledge that a rugged free energy landscape coincides with incomplete occupation of specific M^{2+} binding sites at near-physiological M^{2+} concentrations. Unconventional kinetics in nucleic acid folding frequently encountered in single-molecule experiments are therefore likely to originate from a spectrum of conformations that differ in the occupation of M^{2+} binding sites.

RNA folding | metal ions | heterogeneity | smFRET | NMR

RNA folding is a hierarchical process that depends on the sequential formation of secondary and tertiary structures. As the RNA phosphate-sugar backbone is negatively charged, structural compaction creates electrostatic repulsion, which must be overcome by positive charges. The majority of negative charges are nonspecifically screened by the ion atmosphere, typically a set of dynamically exchanging M^{+} ions (1). An estimated 10–20% of negative charge is, however, compensated by M^{n+} that bind site-specifically to the RNA molecule, in particular, Mg^{2+} (2). One RNA molecule that is known to harbor several specific M^{2+} binding sites is the self-splicing group II intron *Sc*.ai5γ from the yeast mitochondrial *cox1* (cytochrome oxidase 1) gene (3). It is one of the largest known RNA enzymes, and both its folding pathway and catalysis are strictly dependent on Mg^{2+}. In turn, the splicing reaction is inhibited by small amounts of Ca^{2+} (4). Site specificity of the two sequential transesterfication reactions is ensured by proper base pairing between distal exon-binding sites (5′ cleavage, EBS1 and 2; 3′ cleavage, EBS3) and intron-binding sites (IBS1, 2, and 3) (5).

Single-molecule Förster resonance energy transfer (smFRET), i.e., distance-dependent energy transfer between a single pair of fluorophores, is ideally suited to study the cation-dependent conformational dynamics of single RNA molecules (6, 7). If different conformations lead to distinctly different transfer efficiencies, smFRET unveils the entire folding pathway, reports on the relative occurrence of all conformations present in the ensemble, and provides detailed information on the rates at which they interconvert (7). This is important because simple two-state folding is rarely observed in experimental data (8, 9). Rather, the vast conformational space sampled by biomolecules often results not only in folding intermediates but also in kinetic traps and/or multiple native states. In an smFRET experiment, individual molecules consequently display different behaviors that may or may not persist over the observation period (10). Heterogeneity has been precedented for a number of RNA molecules, including group I introns (11, 12), the hairpin ribozyme (13–17), and RNase P RNA (18). In addition, heterogeneity has been reported for different DNA and protein systems (19–24). However, the molecular basis of the phenomenon is often enigmatic, and its quantitative characterization is challenging (21).

Here we use the 5′-exon–intron recognition site of the *Sc*.ai5γ ribozyme to study Mg^{2+}- and Ca^{2+}-mediated RNA–RNA structure formation by smFRET. Additionally, NMR is applied to characterize site-specific M^{2+} binding. In the d3′EBS1*/IBS1* sequence pair used herein, two AUs are replaced by GCs for proper duplex formation, a modification that does not affect the first transesterification step (25, 26). For FRET experiments, the 5′-ends of the d3′EBS1* hairpin and the seven-nucleotide-long IBS1* are labeled with Cy3 and Cy5, respectively (Fig. 1*A*). d3′EBS1* further carries a biotin at its 3′-end for surface immobilization.

Results

Divalent Metal Ions Enhance d3′EBS1*/IBS1* Affinity. The interaction of d3′EBS1* and IBS1* is strictly dependent on M^{2+}

Significance

RNAs are involved in numerous aspects of cellular metabolism, and correct folding is crucial for their functionality. Folding of single RNA molecules can be followed by single-molecule spectroscopy. Surprisingly, it has been found that chemically identical RNA molecules do often not behave identically. The molecular origin of this heterogeneity is difficult to rationalize and the subject of ongoing debate. By combining single-molecule spectroscopy with NMR, we show that heterogeneity is likely to stem from a subset of microscopically different RNA structures that differ with regard to the occupation of divalent metal ion binding sites.

Author contributions: D. Kowerko, S.L.B.K., L.C., and R.K.O.S. designed research; D. Kowerko, S.L.B.K., D. Kruschel, and M.C.A.S.H. performed research; D. Kowerko and R.K.O.S. contributed new reagents/analytic tools; D. Kowerko, S.L.B.K., M.S., and M.C.A.S.H. analyzed data; and D. Kowerko, S.L.B.K., M.S., and R.K.O.S. wrote the paper.

The authors declare no conflict of interest.

This article is a PNAS Direct Submission. D.T. is a guest editor invited by the Editorial Board.

[1]D. Kowerko and S.L.B.K. contributed equally to this work.

[2]Present address: Department of Biochemistry, University of Zurich, 8057 Zurich, Switzerland.

[3]Present address: Department of Medicine, University of Cologne, 50931 Cologne, Germany.

[4]Present address: School of Chemistry, University of Birmingham, Birmingham B15 2TT, United Kingdom.

[5]To whom correspondence should be addressed. Email: roland.sigel@chem.uzh.ch.

This article contains supporting information online at www.pnas.org/lookup/suppl/doi:10.1073/pnas.1322759112/-/DCSupplemental.

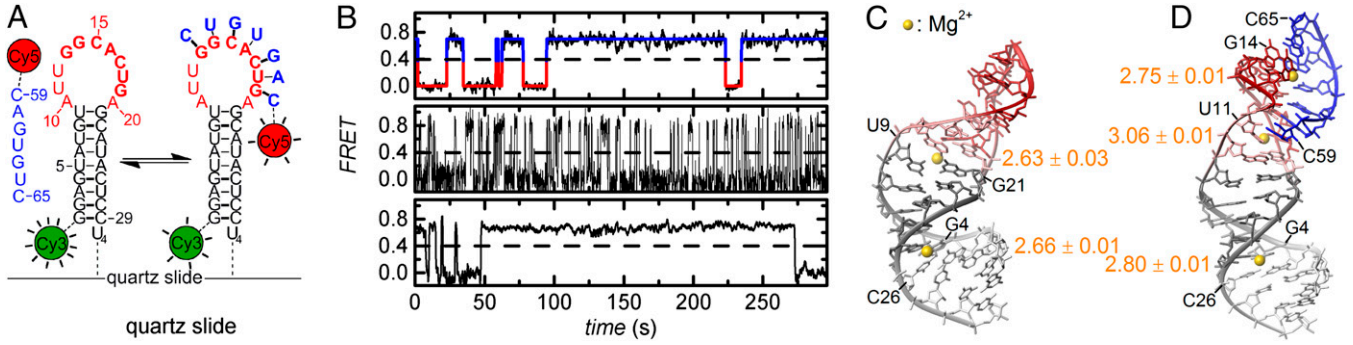

Fig. 1. Studying d3′EBS1*/IBS1* interaction by smFRET and NMR. (*A*) Experimental design for single-molecule fluorescence experiments. Docking of IBS1* onto single surface-immobilized d3′EBS1* molecules is characterized by a concomitant appearance of Cy5 emission due to FRET. (*B*) Representative apparent FRET efficiency time traces revealing fluctuations between the docked state (high FRET) and the undocked state (zero FRET). Thresholding at FRET = 0.4 (dashed line) was used to extract dwell times in the zero FRET state ($t_{zero,i}$, red) and the high FRET state ($t_{high,i}$, blue). (*C* and *D*) d3′EBS1* and d3′EBS1*/IBS1* lowest energy solution structures, each from an ensemble of 200 structures. Yellow spheres indicate Mg^{2+} ions for which the logK_A values are given (26). Structures were prepared using MOLMOL (pdb 2M24 and 2M23) (44).

concentration (25). Native PAGE with the Cy3-d3′EBS1*/Cy5-IBS1* system shows that (*i*) the attached fluorophores do not hamper strand association and (*ii*) M^{2+} further promotes their interaction (*SI Appendix*, Fig. S1). For an in-depth characterization, Cy3-d3′EBS1*/Cy5-IBS1* docking/undocking dynamics were monitored over several minutes, varying either the M^{2+} or the IBS1* concentration. FRET time traces reveal two well-separated FRET states centered around zero (undocked d3′EBS1*) and ∼0.7 (docked d3′EBS1*/IBS1*) (Fig. 1). Control experiments confirmed 1:1 binding stoichiometry and the negligible influence of bleaching and long-lived dark states under the imaging conditions assessed herein (*SI Appendix*, Figs. S2 and S3). Also, tethering fluorophores to RNA and the presence of M^{2+} does not significantly influence their fluorescence spectra, quantum yields, and rotational freedom (*SI Appendix*, Fig. S4). Trajectories were classified as dynamic (type I and II) or static (type IIIa and IIIb) depending on whether interconversion events between these states were present or absent during the observation time of 400 s. Static undocked molecules (type IIIa) were excluded from normalized cumulated FRET histograms (*SI Appendix*, Figs. S5 and S6).

At 100 mM K^+, the docked state is populated on average during 6% of the observation time, and >60% of all molecules remain statically undocked (Fig. 2*A* and *SI Appendix*, Fig. S7). Addition of 100 μM EDTA decreases the docked fraction to <1% and increases the fraction of static undocked molecules to 97.5% (Fig. 2*B*). Upon addition of either 1 mM Mg^{2+} or Ca^{2+}, the high FRET state becomes significantly more populated, and the fraction of type IIIa molecules is reduced to ∼40% (Fig. 2 *D* and *E*). Further addition of up to 8 mM M^{2+} shifts the thermodynamic equilibrium toward the docked state and further decreases the fraction of type IIIa molecules, an effect that is slightly more pronounced for Ca^{2+} than for Mg^{2+} (Fig. 2 *C*–*E*). Further increase of the M^{2+} concentration does not lead to a further shift of the thermodynamic equilibrium. $\Delta G°$ values at physiological M^{2+} concentrations were confirmed by UV spectroscopy, albeit considerable discrepancies were observed at $c(M^{2+}) \geq 25$ mM (Fig. 2 *D* and *E*). The higher propensity of Ca^{2+} to stabilize the interaction of the d3′EBS1*/IBS* complex was confirmed in smFRET experiments conducted at constant M^{2+} concentration: At 8 mM M^{2+} and 40 nM IBS1*, the docked fraction reaches ∼70% (Mg^{2+}) and ∼80% (Ca^{2+}), respectively (*SI Appendix*, Fig. S6).

These data clearly show that 100 mM K^+ alone do not suffice for d3′EBS1*/IBS1* recognition and that interstrand association can be completely abrogated by EDTA-mediated removal of residual M^{2+} in *purissimum* grade KCl (Fig. 2). In turn, increasingly stable interaction and a strong decrease of the fraction of type IIIa molecules are observed at 1 mM ≤ $c(M^{2+})$ ≤ 8 mM. Whether type IIIa molecules have a much lower K_A or correspond to a photophysical artifact was not assessed, but the fact that the fraction of donor-only molecules never falls below ∼20% suggests that these molecules are inactive. This value is consistent with previous reports (27). Prebleached Cy5 may also explain the discrepancies between smFRET and UV melting experiments performed at $c(M^{2+}) \geq 25$ mM (note that the fraction of type IIIa molecules never reaches 0; *SI Appendix*, Fig. S7). Additionally, increasing background noise and uncorrelated docking events in the IBS1* channel were observed at increasing ionic strength, suggesting a local increase of c(IBS1*) in proximity of negatively charged surface. It is likely that this local crowding effect led to further differences between surface-immobilized and freely diffusing molecules, i.e., different $\Delta G°$ values. The results of the thermodynamic analysis are summarized in *SI Appendix*.

Divalent Metal Ions Render d3′EBS1*/IBS1* Interaction Kinetics Multiexponential. To gain insights into the kinetics of docking and undocking, we analyzed the distribution of dwell times extracted from type I trajectories (Fig. 1*B*). The histogram of dwell times in the undocked state recorded in the absence of M^{2+}, i.e., the ensemble-averaged docking process, is satisfactorily described by a monoexponential decay (Fig. 3 and Eq. **9**; $m_{max} = 1$; all equations refer to *SI Appendix*). The fit yields a decay constant of $\tau_{zero} = 73.0$ s ($k_{dock} = 0.55\ \mu M^{-1}{\cdot}s^{-1}$; Eq. **10**). In contrast, the cumulative probabilities of dwell times in the docked state can only be fitted to a multiexponential decay (Fig. 3 and Eq. **9**; $m_{max} = 2$). The resulting decay constants $\tau_{high,1} = 2.9$ s (68%) and $\tau_{high,2} = 7.6$ s (32%) are rather small and reflect the fast decay of the docked state in the absence of M^{2+}. As impurities in the K^+ salt used for imaging buffer preparation significantly affect the interaction of the two strands (*vide supra*), we performed further experiments at 1,000 mM K^+ and 100 μM EDTA (docked fraction = 30%; *SI Appendix*, Fig. S5). Increasing K^+ concentration simultaneously accelerates docking and slows down undocking ($k_{dock} = 1.48\ \mu M^{-1}{\cdot}s^{-1}$, $k_{undock} = 0.061\ s^{-1}$). Single-exponential decay functions describe the experimental data with negligible discrepancies (Fig. 3), suggesting that heterogeneity observed in the absence of EDTA stems for the most part from multivalent impurities. As a control, high-resolution electrospray ionization mass spectrometry experiments were performed, indicating that kinetic heterogeneity is not a result of chemical modification but encoded in the RNA fold (*SI Appendix*, Fig. S8) (17).

In the presence of 100 mM K^+ and 1 mM Mg^{2+}, histograms of dwell times both in the docked and in the undocked state require biexponential fits to be described in a satisfactory fashion (Fig. 3 and Eq. **9**; $m_{max} = 2$). The rate constants indicate that Mg^{2+} increases the docking rate [$k_{dock,1} = 2.40\ \mu M^{-1}{\cdot}s^{-1}$

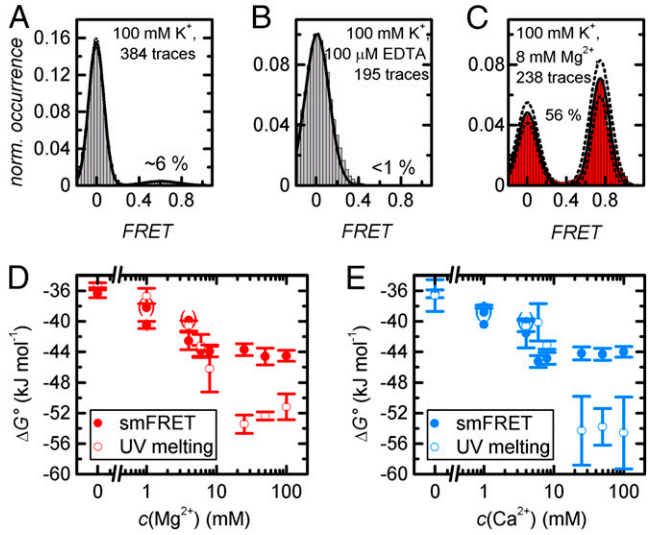

Fig. 2. Analysis of normalized cumulated FRET histograms. (*A*–*C*) Representative data recorded at 100 mM K^+, 100 mM K^+ and 100 µM EDTA, and 100 mM K^+ and 8 mM Mg^{2+}. *B* includes type IIIa molecule (290/295 static undocked). Solid lines correspond to Gaussian fits, and dotted lines denote the SD associated with the amplitude and the width ($2\sigma_{bootstrap}$) (6). (*D* and *E*) Mg^{2+}- and Ca^{2+}-dependent thermodynamic stability of d3′EBS1*/IBS1* as determined by threshold-based analysis of normalized cumulated FRET histograms at FRET = 0.4 (filled circles) and UV thermal melting (open circles). Values in parentheses take into account type IIIa molecules. Error bars associated with smFRET and UV data denote the SD ($3\sigma_{bootstrap}$, 1σ) (6).

(50%), $k_{dock,2}$ = 1.08 $\mu M^{-1}\cdot s^{-1}$ (50%)] and decreases the undocking rate [$k_{undock,1}$ = 0.36 s^{-1} (35%), $k_{undock,2}$ = 0.053 s^{-1} (65%)] (28). Gradual increase of the Mg^{2+} concentration to 8 mM renders the dwell time distributions in the docked and in the undocked state triexponential (Fig. 3 and *SI Appendix*, Fig. S9 and Eq. **9**; m_{max} = 3). Furthermore, the rate associated with docking is increased, whereas undocking is slowed down further. Additional increase of $c(Mg^{2+})$ renders the distribution of dwell times in the undocked state monoexponential and leads to a higher docking rate (Fig. 3; k_{dock} = 2.72 $s^{-1}\cdot\mu M^{-1}$). In turn, the multiexponentiality of dwell time distributions in the docked state persists, and the averaged undocking rate decreases, suggesting a destabilization of the docked state (Fig. 3). Little heterogeneity is observed for dwell time histograms recorded at 10 mM K^+ and 25 mM Mg^{2+} (Fig. 3).

In summary, d3′EBS1*/IBS1* interaction occurs on a single timescale for both the docking and the undocking reaction in the absence of M^{2+}. In turn, multiple timescales are observed at physiological amounts of M^{2+}. At higher M^{2+} concentration, the docking reaction occurs on a single timescale, whereas the undocking reaction persistently occurs on multiple timescales. Similar results were obtained for measurements performed in the presence of 1–100 mM Ca^{2+}. The findings of the dwell time analysis are summarized in *SI Appendix*.

Statistical Description of Intermolecular Heterogeneity. It has been reported earlier that ensemble-averaged dwell time distributions that can be fitted to (roughly) monoexponential decay functions may in some cases erroneously suggest the presence of only two macrostates because they do not take into account molecule-to-molecule variations (21). It is therefore important to compare the behavior of individual molecules. At physiological Mg^{2+} concentrations, we observe time traces with subsecond excursions to the docked and the undocked state (Fig. 1*B*, *Top*), molecules that dwell for several seconds or even minutes in either state (Fig. 1*B*, *Middle*), and a mix between these two extreme behaviors (Fig. 1*B*, *Bottom*). This suggests the presence of kinetic subspecies that may display intermittent conversion on the timescale of the experiment (21, 23). Attempts to correlate thermodynamic and kinetic heterogeneity failed, i.e., intermolecular variations in the high *FRET* value, the docking/undocking rates, and the averaged $\log K_A$ (Fig. 1*B* and *SI Appendix*, S10).

The scatter plot shown in Fig. 4*A* illustrates combinations of docking and undocking rates at 100 mM K^+ and 8 mM Mg^{2+} (21). Bin-free representation of $K_{A,n}$ distributions as semilogarithmic cumulative probability functions $P(\log K_{A,n})$ reveals broad sigmoids covering several orders of magnitude (Fig. 4*B*). As discussed in *SI Appendix*, $\log K_{A,n}$ values follow a beta type distribution, whose width is directly related to the number of dwell times per trace. A numerical approximation of similar distributions has recently been described (12), although analytical solutions have been reported in other fields and can be used to faithfully describe $\log K_{A,n}$ histograms (Eqs. **13** and **14**). Fitting the integral of Eq. **14b** to $P(\log K_{A,n})$ distributions is also possible but in practice rather cumbersome. We therefore extended a logistic-type function previously applied in NMR titrations to describe an equilibrium of the type A + B ⇌ AB (Eq. **16a**) by a shape parameter *p*, which accounts for the number of dwell times per time trace and is determined numerically (Eq. **15d**) (29, 30). Linear combination of s_{max} components yields (Eq. **17b**)

$$P^{norm}\left(\log\left(K_{A,n}\right)\right) = \sum_{s=1}^{s_{max}} a_s \frac{\left(10^{\log\left(K_{A,n}\right)-\log\left(K_{A,s}\right)}\right)^p}{1+\left(10^{\log\left(K_{A,n}\right)-\log\left(K_{A,s}\right)}\right)^p},$$

with $\sum_{s=1}^{s_{max}} a_s = 1$.

As shown in Fig. 4*B*, one-component fit (s_{max} = 1) leads to minor deviations from experimental data recorded in the absence of M^{2+} (p = 1.6 or 2.3; *SI Appendix*, Table S3 and Fig. S15). Hence, the dispersion of $\log K_{A,n}$ values is in the range that is expected for an ergodic system measured for a finite time. In turn, addition of Mg^{2+} leads to considerable discrepancies between one-component fits and experimental $P(\log K_{A,n})$ distributions that cannot be due to finite observation times. Although $P(\log K_{A,n})$ distributions recorded at 10 mM K^+ and 25 mM Mg^{2+} are well approximated using a two-component fit (s_{max} = 2; dotted line in Fig. 4*B*), data recorded at 100 mM K^+ and 8/100 mM Mg^{2+} require three-component fits (s_{max} = 3; dashed lines in Fig. 4*B*). These results suggest that ergodicity is effectively

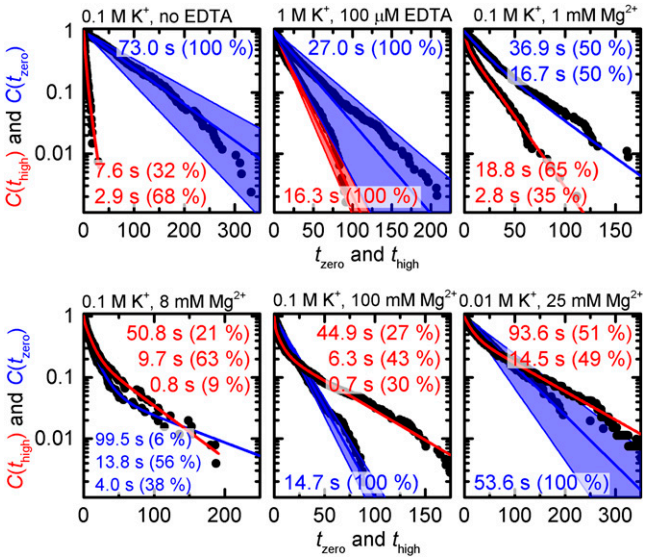

Fig. 3. Dwell time histograms for M^{n+}-dependent IBS1* docking (blue) and undocking (red). Each histogram was fitted to single-exponential or multiexponential decay models as indicated via the number of decay constants. The blue swaths correspond to the bootstrap-estimated SD $2\sigma_{bootstrap}$.

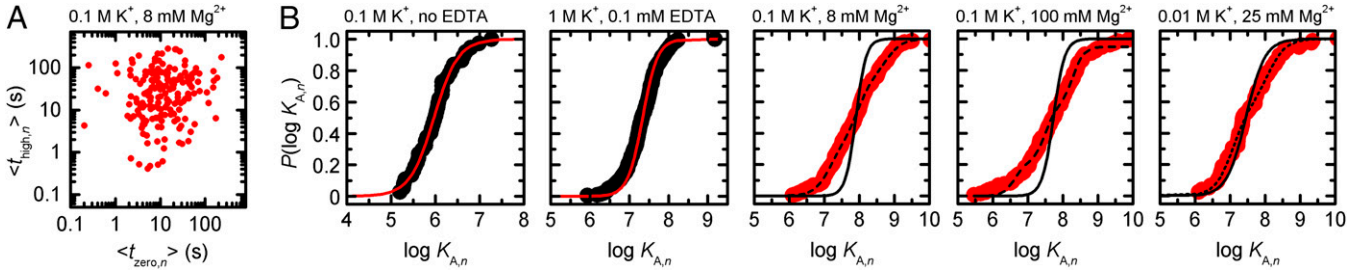

Fig. 4. Distribution of K_A values as determined from smFRET trajectories using Eq. **5b**. (*A*) Scatter plot of the average time spent in the docked and the undocked state, respectively. Each data point corresponds to a single time trace. (*B*) Normalized cumulative probabilities of $\log K_{A,n}$ values determined under various imaging conditions. *Middle* represents the data shown in *A*. Solid lines correspond to logistic fits assuming homogeneous interaction kinetics (Eq. **15d**). Dotted and dashed lines show two- and three-component fits, respectively ($s_{max} \geq 2$; Eq. **17b** and *SI Appendix*, Table S3). For each imaging condition, the intrinsic width of the $\log K_{A,n}$ distribution was accounted for by N: = [Σ ($i_{max,n} + j_{max,n}$)]/2n (*SI Appendix*, Fig. S15).

broken under these conditions (Fig. 4*B*) (21, 31). As a control, heterogeneity of d3′EBS1*/IBS1* interaction in the presence of M^{2+} was confirmed by titrating IBS1* to d3′EBS1* at 8 mM Mg^{2+}: Again, the fractions docked are more adequately represented when three $\log K_A$ values (Eq. **17b**) are taken into account (*SI Appendix*, Fig. S11). Please note that the $\log K_A$ of type IIIb molecules was approximated by a value of 10.

In summary, this section provides the statistical groundwork to analytically describe $K_{A,n}$ distributions from single-molecule experiments as well as a convenient approximation (Eq. **17b**). Hence, we demonstrate that limited observation time is the prime culprit for molecule-to-molecule variations observed in the absence of M^{2+}. Finite observation time cannot, on the other hand, entirely account for heterogeneity observed in the presence of M^{2+}. The fit results are summarized in *SI Appendix*.

Metal Ion Binding Sites in d3′EBS1* and d3′EBS1*/IBS1*. To rationalize the observed heterogeneity, we examined the NMR solution structures of d3′EBS1* and d3′EBS1*/IBS1*, each of which contains several Mg^{2+} binding sites that have been identified by chemical shift perturbation assays (26). In the absence of IBS1*, the EBS1* loop is at least partly unstructured and flexible (Fig. 1*C*). The Mg^{2+} binding site located in the major groove of the d3′ stem near the G4–C26 base pair remains unaffected by the absence or presence of IBS1*. A second binding site is present at the transition between the stem and the loop (A10, A20, and U9–G21 wobble pair). Upon IBS1* docking, EBS1* undergoes a substantial structural rearrangement to form a rigid structure (Fig. 1*D*), thereby also altering M^{2+} binding. The binding site at the loop–stem transition is slightly shifted from the G–U wobble toward the 5′-end of IBS1*, and an additional binding site forms between EBS1* and IBS1* near the first two nucleotides of EBS1*, G13 and G14. We determined the stability constants of Mg^{2+} binding to each site in d3′EBS1* and d3′EBS1*/IBS1* from chemical shift perturbations to be in the low millimolar range ($2.63 \leq \log K_A \leq 3.06$; Fig. 1 *C* and *D*) (32).

To pinpoint the nature of the Mg^{2+}–RNA interaction, we carried out NMR titration studies with Mn^{2+} and $[Co(NH_3)_6]^{3+}$. Mn^{2+} has an ionic radius similar to Mg^{2+} and can coordinate directly (inner sphere) to RNA, causing line broadening of resonances from protons nearby. $[Co(NH_3)_6]^{3+}$ is a kinetically stable mimic of $[Mg(H_2O)_6]^{2+}$ (outer-sphere coordination) (33). NOEs between the NH_3 and RNA protons directly reveal binding. The combination of Mn^{2+} and $[Co(NH_3)_6]^{3+}$ binding thus reveals differences in outer- and inner-sphere coordination of M^{2+}. We find that each site can be occupied by both species (*SI Appendix*, Figs. S12 and S13) but that the two loop binding sites show preference for a specific type of coordination. $[Co(NH_3)_6]^{3+}$ interacts very strongly with the closing G–U wobble in the d3′EBS1* stem, but the interaction is less pronounced in the presence of IBS1*, indicating that the M^{2+} ion docked here must be partially dehydrated for binding when EBS1*/IBS1* is formed. In the EBS1*/IBS1* duplex, both $[Co(NH_3)_6]^{3+}$ and Mn^{2+} interact with G13 and G14. U62–U64 on IBS1* are markedly more affected by $[Co(NH_3)_6]^{3+}$ than by Mn^{2+}. One reason for this may be that the two species bind to EBS1*/IBS1* in a slightly different position because $[Co(NH_3)_6]^{3+}$ is considerably bulkier than Mn^{2+}. The kinked structure of the loop (Fig. 1*E*) may further restrict the accessibility of the phosphate moieties in the EBS1*/IBS1* major groove and of the 5′-end EBS1* nucleotides, which may be regarded as the strongest M^{2+} binding site (2). In conclusion, two M^{2+} are directly involved in EBS1*/IBS1* binding, and M^{2+}–RNA interactions involve (partial) dehydration of M^{2+}.

Estimation of Mg^{2+} Exchange Rates. Ligand exchange in earth alkaline metal aquo complexes occurs at very high rates (10^6 Hz $\leq k_{ex} \leq 10^9$ Hz) (34). On the other end of the spectrum, M^{2+} that are site-specifically bound to RNA are believed to exchange on a timescale of milliseconds because they are (partially) dehydrated and/or the cation makes two or more direct contacts to the RNA (chelation) (2, 35). As discussed in the previous section, the Mg^{2+} ions in proximity to the EBS1*/IBS1* also make multiple contacts. Because direct quantification of Mg^{2+} exchange rates in RNA by ^{25}Mg NMR is challenging (36, 37), we indirectly estimated them by smFRET Mg^{2+} pulse experiments. Here the imaging buffer was depleted of Mg^{2+} at t = 400 s using EDTA, followed by Mg^{2+} replenishment at t = 600 s (t_{tot} = 1,000 s). EDTA functions as a mild denaturing agent that disrupts RNA tertiary structure by coordinating free Mg^{2+} ions, whereas secondary structure is left intact (Fig. 2*B*) (12). Although some time traces revealed instant IBS1* undocking in response to Mg^{2+} removal, a large fraction of d3′EBS1*/IBS1* complexes remained stably docked for many seconds (Fig. 5*A*). In a similar manner, IBS1* docking upon Mg^{2+} readdition often occurred with a delay of several seconds. To estimate the time required to reach the equilibrium, a 2D surface contour plot was built from ∼200 single-molecule time traces (Fig. 5*B*). Thresholding at FRET = 0.4 shows that the undocked fraction reaches steady-state upon removal of Mg^{2+} after ∼200 s ($\tau \sim 40$ s; Fig. 5*C*). In turn, equilibration upon readdition of Mg^{2+} requires ∼50 s ($\tau > 15$ s). Reequilibration is followed by a steady increase of the undocked fraction, a phenomenon mostly likely due to gradual Cy5 photobleaching (*SI Appendix*, Fig. S3). As a consequence, equilibration is consistently slower than the relevant steady-state reactions, i.e., IBS1* undocking in the absence of Mg^{2+} ($\tau < 0.1$ s) and IBS1* docking at 8 mM Mg^{2+} (dominant τ = 13.8 s; Fig. 3).

Recent reports have shown the need to move beyond a static view of biomolecules toward a dynamic description in terms of conformational ensembles (38). In the context of this study, one would expect the RNAs to almost instantaneously undergo a conformational change to relieve the unfavorable electrostatic repulsion created by the removal of a site-specifically bound Mg^{2+} by EDTA. Assuming this behavior, the findings described above could not be explained if Mg^{2+} exchange occurred on a millisecond timescale. Rather, Mg^{2+} exchange is shifted to a time regime resolvable in the smFRET experiment (10^{-2} to 10^2 Hz),

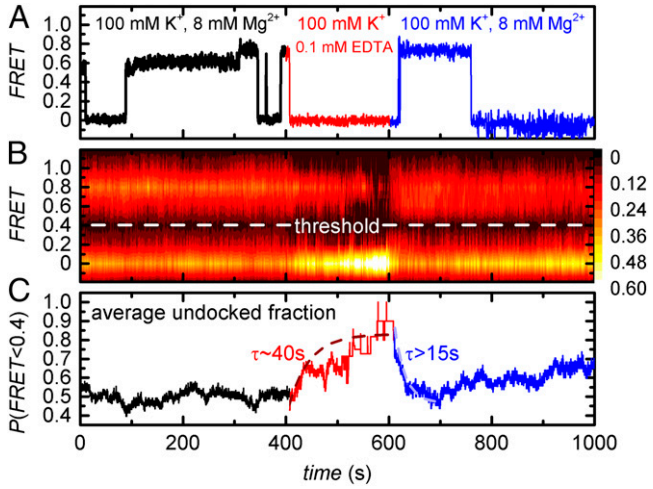

Fig. 5. Mg^{2+} pulse experiments. (*A*) Representative apparent FRET trajectory. (*B*) Two-dimensional surface contour plot of the time-dependent evolution of apparent FRET upon removal and readdition of Mg^{2+}. Graph built from over 200 smFRET time traces. (*C*) Average undocked fraction determined from the data shown in *B*. There was a delay of ~10 s between buffer exchange and the subsequent data acquisition, which was omitted for clarity. τ values correspond to the averaged decay constants obtained by exponential fits.

as the effect of Mg^{2+} association and dissociation is indirectly evidenced by decreased IBS* docking/undocking rates.

Discussion

This study combines smFRET and NMR to address the influence of Mg^{2+} and Ca^{2+} on the structural dynamics of the d3′EBS1*/IBS1* sequence pair derived from the group II intron *Sc*.ai5γ. The occurrence of the docked state is found to be strongly M^{2+}-dependent, confirming earlier reports (25). d3′EBS1*/IBS1* interaction dynamics occur on a single timescale in the absence of M^{2+}, whereas multiple timescales and nonergodic behavior are observed at 1–8 mM M^{2+}. Broken ergodicity is persistent at higher M^{2+} concentrations, although IBS1* docking occurs on a single timescale. NMR experiments show that two specific M^{2+} binding sites are located in proximity to the d3′EBS1*/IBS1* duplex, probably resulting in multidentate binding and (partial) dehydration of the M^{2+} ions. Mg^{2+} pulse experiments further indicate that the exchange rates of these M^{2+} is likely to fall into the typical time resolution of an smFRET experiment. Hence, this study not only addresses the M^{2+}-dependence of kinetic heterogeneity in RNA tertiary structure formation, it also provides a rigorous characterization of specific M^{2+} binding to the RNA.

The simplest conceivable free energy landscape model is a two-state reaction over a single transition state barrier. Here the probability distribution of the dwell times is monoexponential, and the rate of decay is determined by the height of the energy barrier (39). The energy barrier associated with d3′EBS1*/IBS1* docking and undocking in the absence of M^{2+} depends to a large extent on how effectively the ion atmosphere screens the electrostatic potential building up when the two RNAs are close in space (1). In contrast, multiexponential kinetics and broken ergodicity in the presence of low millimolar amounts of M^{2+} suggests a rugged energy landscape with more than one thermodynamically stable d3′EBS1* and d3′EBS1*/IBS1* conformation (40). Heterogeneity is most pronounced when site-specific M^{2+} binding pockets are on average half occupied, i.e., M^{2+} concentrations between 1 mM and 8 mM (Figs. 3 and 4). Hence, we propose that the phenomenon is largely due to differences in M^{2+} binding (Fig. 6). All substructures display distinct docking/undocking kinetics and may interconvert at the cation exchange rates α_m and β_n ($m,n = -4,\ldots-1,1,\ldots,4$), which are likely to fall into a time regime resolvable by the CCD camera. In agreement with this model, IBS1* docking becomes monoexponential at 100 mM M^{2+}. On the other hand, the heterogeneity associated with IBS1* undocking and nonergodic behavior is persistent under these conditions, seemingly contradicting this working model. One possible explanation is the fact that high ionic strength is known to reduce the affinity of Mg^{2+} toward specific binding sites; that is, the latter could, in fact, not be saturated at 100 mM M^{2+} (1). However, nonspecific interaction of IBS1* with the surface as well as discrepancies between surface-immobilized (smFRET) and freely diffusing molecules (UV) under these conditions suggests that persistent heterogeneity is most likely caused by M^{n+}-mediated interaction of RNA with the surface and/or local crowding effects. Control experiments further support this hypothesis: (*i*) Usual levels of background noise and few nonspecific IBS1* binding events are observed at 10 mM K^+ and 25 mM Mg^{2+}, a concentration that is expected to saturate the M^{2+} binding sites. Even though intermolecular heterogeneity is also present, it is considerably less pronounced. (*ii*) Freely diffusing d3′EBS1* and IBS1* molecules coencapsulated within surface-tethered lipid vesicles almost exclusively populate the docked state and do not show any sign of heterogeneity at 50 mM Mg^{2+}. It should be noted, however, that Cy3/Cy5 coblinking events and limited observation time preclude rigorous kinetic analysis (*SI Appendix*, Fig. S16) (41). In conclusion, our data suggest that the M^{2+}-induced kinetic heterogeneity associated with d3′EBS1*/IBS1* docking and undocking is due to 2^n structural permutations resulting from n incompletely occupied M^{2+} binding pockets.

Conclusion

Even though heterogeneity is frequently observed in single-molecule studies addressing nucleic acid folding, discord persists with regard to the origin of the phenomenon (11–18). Lee et al. (42) have proposed a model that explains multiexponential kinetics in the dissociation of an artificial triplex DNA by the coexistence of metastable states that interconvert when ssDNA slides along the major groove of dsDNA. A correlation between heterogeneity and the availability of M^{n+} has been reported for several native nucleic acids, including RNase P RNA and the human telomeric G-quadruplex (18, 22). It has been speculated (but never been proven) that kinetic heterogeneity associated with G-quadruplex conformational dynamics stems from incomplete occupation of M^{n+} binding sites, leading to a pronounced

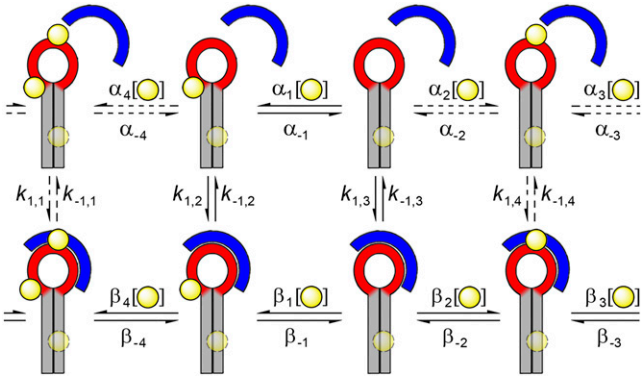

Fig. 6. Working model of M^{2+}-dependent d3′EBS1*/IBS1* interaction kinetics. Several d3′EBS1* conformers differing in M^{2+} occupancy coexist at physiological Mg^{2+} or Ca^{2+} concentrations, and they interconvert at the cation exchange rates (α, β). Conformers further differ with regard to IBS1* docking and undocking kinetics (k_1, k_{-1}). The d3′-stem binding site (faint circle near G4–C26) is assumed to have little influence on k_1 and k_{-1}. M^{2+} binding sites are depicted as yellow spheres. Dashed lines indicate equilibria that were not detected directly.

memory effect (22). K^+ exchange in the bimolecular DNA G-quadruplex $d(G_4T_4G_4)_2$ has been estimated to occur on a timescale of seconds using ^{205}Tl NMR, a timescale relevant for most single-molecule experiments (43).

In this study, we provide direct evidence that kinetic heterogeneity in nucleic acid folding can be caused by incomplete occupation of specific M^{n+} binding sites. M^{n+} ions have been identified in numerous nucleic acid structures, and they typically display millimolar affinities for their binding sites (34, 36, 37). As a consequence, these sites are not fully occupied at physiological M^{n+} concentrations, providing a possible explanation for the heterogeneity observed in the majority of single-molecule studies addressing DNA and RNA folding.

Materials and Methods

RNA Preparation. RNA sequences for smFRET were purchased from Microsynth AG and PAGE- and RP-HPLC–purified. Sequences used in NMR experiments were transcribed in vitro (26).

Electrophoresis, UV, and Mass Spectrometry. Please refer to *SI Appendix*.

smFRET Experiments. d3′EBS1* was immobilized within a microfluidic channel, whereas IBS1* was free in solution. Donor and acceptor emissions were monitored over 400 s using total internal reflection fluorescence microscopy and a CCD camera (10 frames per s). Please refer to *SI Appendix* for further details.

NMR. All spectra were recorded on a Bruker Avance 700-MHz spectrometer with a 5-mm CRYO TXI inverse triple-resonance probe head with z-gradient coil. Mg^{2+} titrations are described in ref. (26). Mn^{2+}-induced line broadening was followed in a series of $[^1H,^1H]$-NOESY spectra recorded in 100% D_2O at 293 K for d3′EBS1* and 298 K for d3′EBS1*/IBS1*. For M^{2+} titrations, $MnCl_2$ was added up to a final concentration of 300 μM (d3′EBS1*) and 360 μM (d3′EBS1*/IBS1*). Line broadening of individual peaks was assessed visually using Sparky (www.cgl.ucsf.edu/home/sparky/). NOE cross-peaks between $[Co(NH_3)_6]^{3+}$ and d3′EBS1* or d3′EBS1*/IBS1* were assigned in $[^1H,^1H]$-NOESY spectra recorded in 90% H_2O/10% D_2O at 278 K.

ACKNOWLEDGMENTS. The authors thank Richard Börner, Rahel Bucher, Achilles N. Kapanidis, Mokrane Khier, Madhavi Krishnan, David Rueda, and Ben Schuler for insightful discussions. This work was supported by the Forschungskredit of the University of Zurich (UZH) (to D. Kowerko, S.L.B.K., and M.C.A.S.H.), the Boehringer Ingelheim Fonds (BIF FUTURA 2/2005, 112, to D. Kruschel), and the European Research Council (MIRNA259092, to R.K.O.S.).

1. Lipfert J, Doniach S, Das R, Herschlag D (2014) Understanding nucleic acid-ion interactions. *Annu Rev Biochem* 83:813–841.
2. Freisinger E, Sigel RKO (2007) From nucleotides to ribozymes—A comparison of their metal ion binding properties. *Coord Chem Rev* 251(13-14):1834–1851.
3. Sigel RKO, Vaidya A, Pyle AM (2000) Metal ion binding sites in a group II intron core. *Nat Struct Biol* 7(12):1111–1116.
4. Erat MC, Sigel RKO (2008) Divalent metal ions tune the self-splicing reaction of the yeast mitochondrial group II intron Sc.ai5gamma. *J Biol Inorg Chem* 13(6):1025–1036.
5. Pyle AM (2010) The tertiary structure of group II introns: Implications for biological function and evolution. *Crit Rev Biochem Mol Biol* 45(3):215–232.
6. König SLB, et al. (2013) BOBA FRET: Bootstrap-based analysis of single-molecule FRET data. *PLoS ONE* 8(12):e84157.
7. Roy R, Hohng S, Ha T (2008) A practical guide to single-molecule FRET. *Nat Methods* 5(6):507–516.
8. Steiner M, Karunatilaka KS, Sigel RKO, Rueda D (2008) Single-molecule studies of group II intron ribozymes. *Proc Natl Acad Sci USA* 105(37):13853–13858.
9. Steiner M, Rueda D, Sigel RKO (2009) Ca^{2+} induces the formation of two distinct subpopulations of group II intron molecules. *Angew Chem Int Ed Engl* 48(51):9739–9742.
10. König SLB, Kowerko D, Sigel RKO (2013) Kinetic subpopulations detected by single-molecule spectroscopy: Fundamental property of functional nucleic acids or experimental artefact? *Chimia (Aarau)* 67(4):240–243.
11. Zhuang X, et al. (2000) A single-molecule study of RNA catalysis and folding. *Science* 288(5473):2048–2051.
12. Solomatin SV, Greenfeld M, Chu S, Herschlag D (2010) Multiple native states reveal persistent ruggedness of an RNA folding landscape. *Nature* 463(7281):681–684.
13. Zhuang X, et al. (2002) Correlating structural dynamics and function in single ribozyme molecules. *Science* 296(5572):1473–1476.
14. Okumus B, Wilson TJ, Lilley DMJ, Ha T (2004) Vesicle encapsulation studies reveal that single molecule ribozyme heterogeneities are intrinsic. *Biophys J* 87(4):2798–2806.
15. Tan E, et al. (2003) A four-way junction accelerates hairpin ribozyme folding via a discrete intermediate. *Proc Natl Acad Sci USA* 100(16):9308–9313.
16. Rueda D, et al. (2004) Single-molecule enzymology of RNA: Essential functional groups impact catalysis from a distance. *Proc Natl Acad Sci USA* 101(27):10066–10071.
17. Ditzler MA, Rueda D, Mo J, Håkansson K, Walter NG (2008) A rugged free energy landscape separates multiple functional RNA folds throughout denaturation. *Nucleic Acids Res* 36(22):7088–7099.
18. Qu X, et al. (2008) Single-molecule nonequilibrium periodic Mg^{2+}-concentration jump experiments reveal details of the early folding pathways of a large RNA. *Proc Natl Acad Sci USA* 105(18):6602–6607.
19. Brujic J, Hermans ZRI, Walther KA, Fernandez JM (2006) Single-molecule force spectroscopy reveals signatures of glassy dynamics in the energy landscape of ubiquitin. *Nat Phys* 2(4):282–286.
20. Hyeon C, Hinczewski M, Thirumalai D (2014) Evidence of disorder in biological molecules from single molecule pulling experiments. *Phys Rev Lett* 112(13):138101.
21. Hyeon C, Lee J, Yoon J, Hohng S, Thirumalai D (2012) Hidden complexity in the isomerization dynamics of Holliday junctions. *Nat Chem* 4(11):907–914.
22. Lee JY, Okumus B, Kim DS, Ha T (2005) Extreme conformational diversity in human telomeric DNA. *Proc Natl Acad Sci USA* 102(52):18938–18943.
23. Liu B, Baskin RJ, Kowalczykowski SC (2013) DNA unwinding heterogeneity by RecBCD results from static molecules able to equilibrate. *Nature* 500(7463):482–485.
24. Lu HP, Xun L, Xie XS (1998) Single-molecule enzymatic dynamics. *Science* 282(5395):1877–1882.
25. Kruschel D, Sigel RKO (2008) Divalent metal ions promote the formation of the 5′-splice site recognition complex in a self-splicing group II intron. *J Inorg Biochem* 102(12):2147–2154.
26. Kruschel D, Skilandat M, Sigel RK (2014) NMR structure of the 5′ splice site in the group IIB intron Sc.ai5γ—Conformational requirements for exon-intron recognition. *RNA* 20(3):295–307.
27. Ha T, Tinnefeld P (2012) Photophysics of fluorescent probes for single-molecule biophysics and super-resolution imaging. *Annu Rev Phys Chem* 63:595–617.
28. Skilandat M, Sigel RKO (2014) The role of Mg(II) in DNA cleavage site recognition in group II intron ribozymes: Solution structure and metal ion binding sites of the RNA-DNA complex. *J Biol Chem* 289(30):20650–20663.
29. Britton NF (2003) Single species population dynamics. *Essential Mathematical Biology*, ed Britton NF (Springer, Berlin), pp 1–40.
30. Mitchell PR (1979) Hydrophobic interactions in ternary Zinc(II) and Copper(II) complexes containing 1,10-phenanthroline or 2,2′-bipyridyl and an alkane carboxylate or sulphonate. *Dalton Trans* 1979(5):771–776.
31. Greenfeld M, Pavlichin DS, Mabuchi H, Herschlag D (2012) Single Molecule Analysis Research Tool (SMART): An integrated approach for analyzing single molecule data. *PLoS ONE* 7(2):e30024.
32. Erat MC, Sigel RKO (2007) Determination of the intrinsic affinities of multiple site-specific Mg(2+) ions coordinated to domain 6 of a group II intron ribozyme. *Inorg Chem* 46(26):11224–11234.
33. Rowinska-Zyrek M, Skilandat M, Sigel RKO (2013) Hexaamminecobalt(III) - probing metal ion binding sites in nucleic acids by NMR. *Z Anorg Allg Chem* 639(8-9):1313–1320.
34. Pechlaner M, Sigel RKO (2012) Characterization of metal ion-nucleic acid interactions in solution. *Met Ions Life Sci* 10:1–42.
35. Chu VB, Bai Y, Lipfert J, Herschlag D, Doniach S (2008) A repulsive field: Advances in the electrostatics of the ion atmosphere. *Curr Opin Chem Biol* 12(6):619–625.
36. Cowan JA (1991) Coordination chemistry of Mg^{2+} and 5S rRNA (Escherichia coli): Binding parameters, ligand symmetry, and implications for activity. *J Am Chem Soc* 113(2):675–676.
37. Reid SS, Cowan JA (1990) Biostructural chemistry of magnesium ion: Characterization of the weak binding sites on tRNA(Phe)(yeast). Implications for conformational change and activity. *Biochemistry* 29(25):6025–6032.
38. Yang S, Salmon L, Al-Hashimi HM (2014) Measuring similarity between dynamic ensembles of biomolecules. *Nat Methods* 11(5):552–554.
39. Lannon H, Vanden-Eijnden E, Brujic J (2012) Force-clamp analysis techniques give highest rank to stretched exponential unfolding kinetics in ubiquitin. *Biophys J* 103(10):2215–2222.
40. Greenfeld M, Solomatin SV, Herschlag D (2011) Removal of covalent heterogeneity reveals simple folding behavior for P4-P6 RNA. *J Biol Chem* 286(22):19872–19879.
41. Cordes T, et al. (2010) Sensing DNA opening in transcription using quenchable Förster resonance energy transfer. *Biochemistry* 49:9171–9180.
42. Lee I-B, Hong S-C, Lee NK, Johner A (2012) Kinetics of the triplex-duplex transition in DNA. *Biophys J* 103(12):2492–2501.
43. Gill ML, Strobel SA, Loria JP (2005) ^{205}Tl NMR methods for the characterization of monovalent cation binding to nucleic acids. *J Am Chem Soc* 127(47):16723–16732.
44. Koradi R, Billeter M, Wüthrich K (1996) MOLMOL: A program for display and analysis of macromolecular structures. *J Mol Graph* 14(1):51–55, 29–32.